Journal of Metals, Materials and Minerals, 35(2), e2279, 2025

Photodegradation of Malachite green using 2D g-C_3N_5 nanosheet: A promising metal free catalyst

Sonali BISWAL[1], Asima SUBHADARSHINI[2], Swayam Aryam BEHERA[1], P. Ganga Raju ACHARY[1,*] and Binita NANDA[1,*]

[1] *Department of Chemistry, Faculty of Engineering and Technology (ITER), Siksha 'O' Anusandhan (Deemed to be) University, Bhubaneswar, Odisha, 751030 India*

[2] *Department of Chemistry, Environmental sciences, Faculty of Engineering and Technology (ITER), Siksha 'O' Anusandhan (Deemed to be) University, Bhubaneswar, Odisha, 751030 India*

***Corresponding author e-mail**: binitananda@soa.ac.in

Received date:
30 December 2024
Revised date:
23 January 2025
Accepted date:
4 April 2025

Keywords:
Carbon nitride;
Cationic dye;
Water remediation;
Advanced oxidation processes

Abstract

Environmental issues have become more serious these days due to the growth of modern industries. The paper and textile industries, in particular, were heavily dependent on the printing and discharge of dye, which constantly leaked into the water ecology and constituted a serious risk to public health. Organic wastewater treatment and remediation for its associated risks have received a lot of attention lately. This work explored the potential of the g-C_3N_5 nanostructure as a novel photocatalyst for malachite green degradation in aqueous solution while exposed to visible light. The nanocomposite was fabricated through an ultrasonicate-assisted technique. A number of analysis techniques, such as CHNS, XRD, FTIR, UV-DRS, SEM, Electrical, and XPS were employed to verify the successful fabrication of the photocatalyst. At pH 6.5, the catalyst dose of 0.06 g·L^{-1}, with malachite green concentration of 20 mg·L^{-1}, and in a reaction period of 90 min, the degradation efficiency had been found to be 88%. The produced hydroxyl radicals ($OH^{\bullet}$) is considered to be major scavenger for degradation of malachite green. The above method suggested an easy, environmentally friendly and practical approach to produce excellent photocatalytic 2D g-C_3N_5 nanosheet for environmental cleanup

1. Introduction

The quick advancement of textile industries has remarkable environmental concern, which has led in increase in the dissolution of untreated dye containing waste water into water bodies. These results in toxicity, colouration, oxygen depletion, bioaccumulation. The chemical composition of dye includes aromatic hydrocarbon, heterocyclic compounds, heavy metals such as Cr, Cu, Pb which can act as carcinogens due to azo group present in it. It also affects the physiological disruption in human body. The aquatic life is harmed by increasing BOD, which has decreased oxygen content as well as hinder the photosynthetic activity of aquatic plants. Organic pollutants offer a threat to biological systems and the environment due to their non-biodegradable nature. Among the many harmful dyes in textile dye waste are malachite green, methylene blue and Congo red. The paper, leather and textile industries use cationic dye like Malachite green which is highly toxic causing serious illness in human [1]. Malachite green (MG) is both a triphenylmethyl colour and an antibacterial medication for animals. Additionally, it is frequently employed globally in aquaculture as a fungicide and parasiticide. Based on studies, even small quantity of malachite green discharged into preserved water may suffer a large range of toxicological impacts on several kinds of fish and some animals [2]. As being non-biodegradable Malachite green can not be eliminated from aqueous solutions. In order to get rid from these emerging methods such as adsorption, membrane filtration, ion exchange, chemical oxidation and photocatalytic degradation methods has been used [3-5]. As visible light radiation includes more than 40% solar radiation and UV radiation, the photocatalytic degradation process prefers visible radiation rather than ultra violet radiation. It has been seen that, to eliminate organic pollutants producing CO_2, mineral salts, photocatalyst has proved an effective technique in this regard [6-9]. The development of ultraviolet (UV) and visible light-based advanced oxidation processes (AOPs) has been the focus of much research [10,11]. As sunlight has a large wavelength range, its infinity of energy can be utilized to activate photocatalysts [12-15]. Semiconductor photocatalyst such as TiO_2, ZnO, ZnS has been taken an important role harvest solar energy to improvise this issue. However, due to their quick recombination and low adsorption range of visible light, their significance is still limited. A novel polymeric material called graphitic carbon nitride (g-C_3N_4) is widely applied in a range of environmental applications having unusual arrangement of SP^2 created a tris-S triazine ring linked to tertiary amines by hybridizing carbon and nitrogen atoms [16]. Their excellent visible light receptivity (band gap nearly 2.7 eV) allows it to be optimal for a wide range of photochemical reactions [17]. Although its photocatalytic stability is restricted by rapid recombination rate and a short half-life of a photo-

generated charge carriers. Many strategies including heterojunction creation, noble metal doping and morphological control have been attempted to enhance the photocatalytic efficiency of g-C_3N_4 [18]. However, is challenging to regulate the proper doping form, which makes chemical doping in CN materials difficult to do. To the best of our knowledge, incorporating nitrogen into the carbon matrix of CNs helps to improve field emission, photo and basic catalysis, carbon capture, and storing of energy capabilities in addition to a smaller band gap. Therefore, an alternative approach for predicting extended versatile properties is to develop nitrogen-rich CN materials [19]. Wang *et al.* have used nano hard templating in recent years and changed the π conjugated system with a long electron pair on the nitrogen atom in the heptazine motif [20]. S. Etal has successfully produced C_3N_5 altered carbon nitride structure thermally deamination of 2,5,8-trihydrazino-s-heptazine [21-24]. The mesoporous g-C_3N_5 was produced using nitrogen enriched 3-amino-1,2,4-triazole, larger C/N ratio, narrower band gap (2.2 eV), the existence of azo-bridged aromatic compounds and azo chromophores (−N=N−) in combination with aromatic compounds, has broadened the visible light absorption range and improved catalytic performance [25-27].

2. Experimental section and characterization

2.1 Synthesis of g-C_3N_5 nanosheet

Ammonium chloride (NH_4Cl) 5 g and 3-amino-1,2,4-triazole (3-AT) 5 g were combined and ground into a homogenous solid mixture, which underwent three hours of heating to 500°C, ramping to produce the bulk C_3N_5 nanoparticles at a rate of 10°C·min^{-1}. The dark briskish brown substance known as bulk g-C_3N_5 was obtained after naturally cooling [28]. By KBr-assisted ultrasound exfoliation the g-C_3N_5 nanosheets were obtained, 0.6 g of as-synthesized bulk g-C_3N_5 100 mL of a 10 mmol KBr solution was mixed with powder, and the mixture was agitated using an ultrasonic device for another two hours for the synthesis of the nanosheets. After centrifuging the mixture at 8000 rpm, the excess bromide ions were washed off. Then it was dried at 80°C for 12 h, ground and named as g-C_3N_5 nanosheet [29].

2.2 Characterization

The organic elemental analyser Unicube was used for estimating the CHNS value. At λ = 1.5406 Å CuKα radiation, X-ray diffraction (XRD) had been recorded with a Rigaku Mini flex diffractometer having a scanning range of 10° to 80°. The functional group were characterised using the Jasco FT/IR-4600LE for Fourier transforms infrared spectrograph (FTIR). Boric acid was employed as a reference for (UV-DRS) spectra in 200 nm to 800 nm range utilizing the Jasco-750-UV-VIS spectrophotometer. The JEOL-6390 Scanning electron microscope (SEM) was applied to examine the surface morphologies. A Kratos Axis-165 (XPS) spectrophotometer with a MgK source was utilized for X-ray photoelectron spectroscopy. To analyse electrical behaviour, an LCR meter of model no.N4L PSM, 1735 is utilized. Vario TOC select (Elementar, Germany) with HTC oxidation and DE/ multi-N/C (Jena, Germany) with UVP for Total organic carbon (TOC) estimation.

2.3 Photocatalytic experiment

Under solar light irradiation, photocatalytic experiments are conducted with an average light intensity of 100000 lx. Preparing catalyst of 0.02 g in 20 mL of 20 ppm Malachite Green (MG) with constant stirring. The adsorption- desorption equilibrium has been maintained by stirring in a dark place for a period of 30 min prior to exposing the solution to the sunlight for 90 min. By centrifuging the suspension, the resulting was collected, once the reaction was finished. The UV–Visible spectrophotometer was used to analyse the solution mentioned above. Using Beer-Lambert's equation, the absorbance at 614 nm was used to calculate the concentration of the MG solution. The percentage of decolorization efficiency was computed using the following Equation (1).

$$\text{Decolorization percentage (\%)} = (C_0 - C)/C_0 \times 100 \quad (1)$$

Initial concentration (before degradation) is denoted by C_0 at time t = 0, while the solution's final concentration (after degradation) is referred to by 'C' at time t = t.

3. Result and discussion

3.1 CHNS analysis

CHNS elemental analysis of the synthesised g-C_3N_5 was carried for analyzing the composition. The result indicated 68.6 wt% nitrogen, 29.4 wt% carbon and 1.80 wt% hydrogen indicating an empirical formula of $C_3N_{5.4}H_2$ that was in close proximity to the theoretical weight percentage of g-C_3N_5. Resulting in confirmation of formation of g-C_3N_5 [32].

3.2 X-ray diffraction (XRD) analysis

Figure 1 showed the XRD pattern of the g-C_3N_5 samples. The peak positioned at 13.1° corresponds (100) plane, which is a unique feature of in plane slacking, suggests distortion in carbon nitride framework and enlargement of azo (-N=N-) bridging between heptazine units connection causes nanochannel gap [31]. In addition, the diffraction plane (002) has been shifted to the peak value at 2θ = 27.3° confirming the conjugated aromatic CN framework's crystallinity and interlayer stacking inside the wall structure, which has enhanced transfer of charges generated by photolysis.

The crystallite size for g-C_3N_5 was calculated to be of 7.26 nm through the Scherrer Equation (2).

$$D = \frac{K\lambda}{\beta \, Cos\theta} \quad (2)$$

where k is 0.9 (Scherrer's constant), λ is incident rat of CuKα (1.5404 Å), β is the FWHM, θ is Bragg's diffraction angle, and D is the average crystallite size, along with the interplanar spacing of 0.206 nm , which explains the minor rise in 2θ and d spacing in the repulsion between electron rich p conjugated g-C_3N_5 nanosheets [30,32] that is determined from the Bragg's law representing the Equation (3),

$$2d\ Sin\theta = n\lambda \quad (3)$$

where d is the spacing of crystal layers, θ is the incident angle, n is an integer and λ is the x-ray wavelength. which explains the minor rise in 2θ and d spacing in the repulsion between electron rich p conjugated g-C_3N_5 nanosheets.

3.3 FTIR analysis

The chemical states in the examining the characteristics of nanomaterials is also an essential parameter. As the results, FTIR analysis was used to investigate the element component of g-C_3N_5. Adsorbed water molecules –NH_2 and –OH on the surface created the stretching vibration absorption peak, which is roughly 3100 cm^{-1} [33,34]. The characteristic stretching vibration of heterocyclic CN units gave rise to the band ranging from 1650 cm^{-1} to 1250 cm^{-1}. An additional prominent peak located approximately at 802 cm^{-1} signified the triazine units breathing vibration confirming the formation of g-C_3N_5 nanosheet as shown in Figure 2.

3.4 SEM analysis

The surface morphology of g-C_3N_5 nanosheet was shown in Figure 3(a). which shows highly porous and 2-D sheet like structure along with EDAX as displayed in Figure 3(b). showing the availability of elements like carbon, nitrogen and oxygen [35]. The histogram curve as shown in Figure 3(c). for g-C_3N_5, with mean particle size of 116.5 nm. These results validated the formation of porous 2D nanosheet of g-C_3N_5.

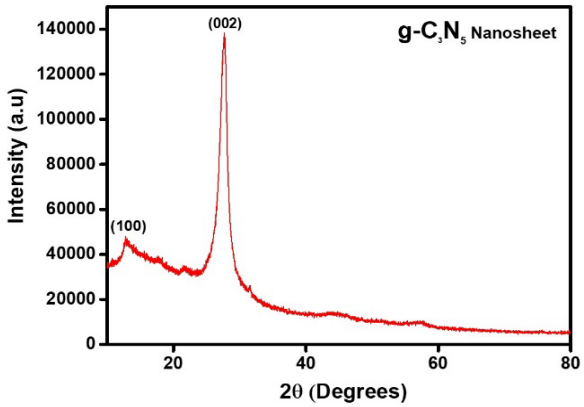

Figure 1. XRD analysis of g-C3N5.

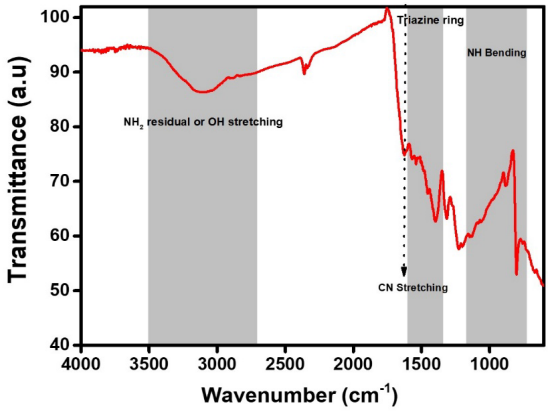

Figure 2. FTIR analysis of g-C_3N_5.

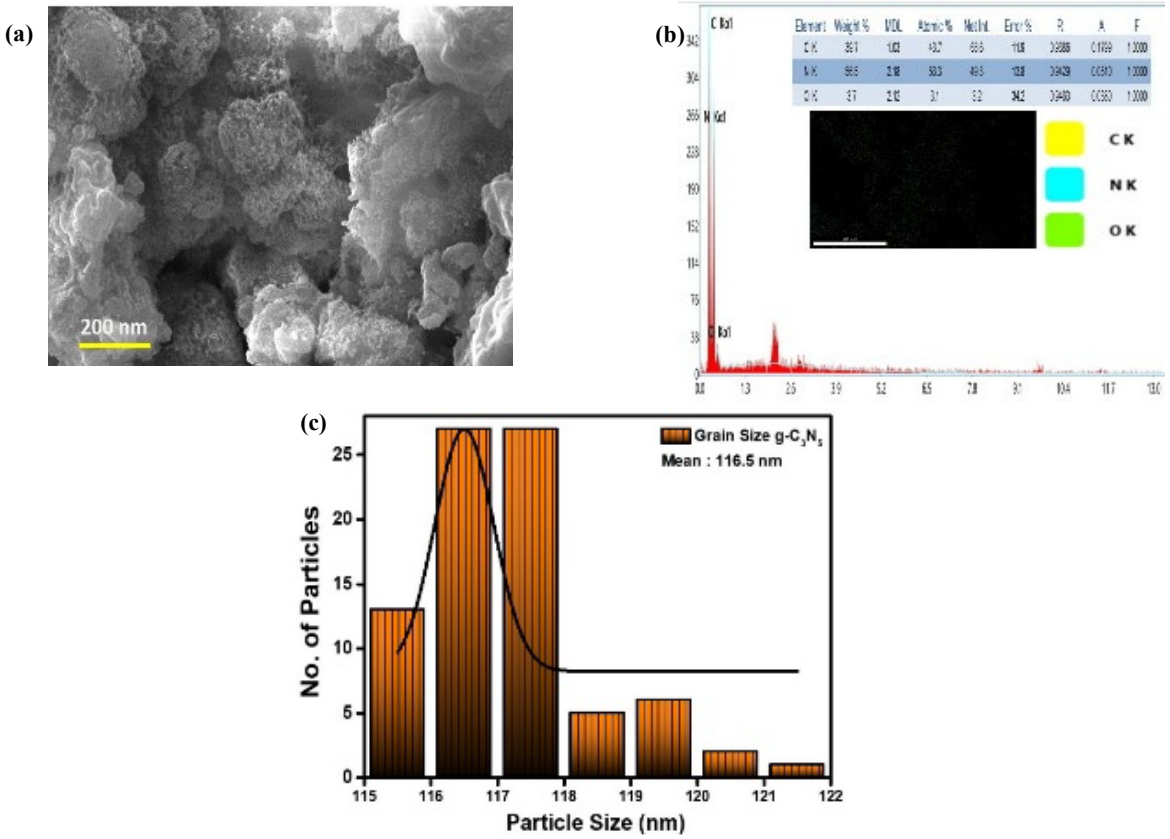

Figure 3. (a) SEM image, (b) Elemental mapping with EDS, and (c) Histogram graph for particle size distribution of g-C_3N_5 nanosheet.

3.5 UV-DRS analysis

Figure 4(a) displays the UV-Vis DRS spectra of g-C_3N_5, which demonstrate the considerable UV-Vis absorption due to a longer π conjugated network. The n—π* transition, which requires the excitation of electrons from nitrogen nonbonding nitrogen orbital to conjugated π* orbital is responsible for large adsorption peak observed at 393 nm in the UV-Vis spectra of g-C_3N_5 [21]. Because of the overlap between N 2p heptazine π conjugated molecules and N 2p orbitals of bridging azo moieties, an extended π conjugated network resulted in a red shifted absorption spectra of g-C_3N_5 exhibiting tailing the band up to 670 nm [36]. The delocalised aromatic π conjugated system of residual –NH_2 group has upshifted valence band's location and π—π* transition results with a comparatively low energy which makes it easier for a substantial amount of visible spectrum to be absorbed and causes the sample to appear orange. The photocatalytic effect of a semiconductor essentially depends upon the electronic band gap configuration. The relationship between absorbance and incoming photon energy is seen in Equation (4).

$$(\alpha h\upsilon)^{1/m} = C(h\upsilon - E_g) \quad (4)$$

Using a graph of $(\alpha h\upsilon)^{1/2}$ vs. hυ, the linear tangent to abscissa can be calculated, where α is the absorption coefficient, the plank constant, and υ is the frequency of light, E_g is the bandgap and C is absorption constant. Using Tauc plot, materials optical band gap can be calculated in two ways either directly ($\alpha h\upsilon^2$ vs. hυ) when m = ½ or indirectly when m = 2 [37-39]. By extrapolating the linear portion to the energy axis, the band gap E_g was determined to be 1.90 eV as shown in Figure 4(b).

3.6 XPS analysis

Figure 5(a) shows the chemical state of prepared g-C_3N_5 as shown by XPS. The synthesized g-C_3N_5 nanocomposite verified the presence of C, N, O through survey curve. According to XPS, individual peaks for the elements with the high resolution as shown in Figure 5(b-d). The intermediate of C-C and the SP^2 hybrid aromatic ring of N-C=N having binding energy 284.8 eV and 281.7 eV respectively. Along with the typical peak at 286.6 eV represents C-O for C1s. Two typical peaks are representing to the N1s high resolution spectra where the SP^2 hybridised aromatic ring C=N-C and tertiary–$(C)_3$ having binding energy 398.1 eV and 396.3 eV respectively, this confirms the formation of heptazine unit with azo linkages [40,41]. The O1s peak at 528.65 eV is attributed to surface-bound oxygen, including adventitious oxygen and hydroxyl (–OH) groups.

3.7 Electrical analysis

As shown in Figure 6(a) the dielectric constant of g-C_3N_5, decreases with an increase in frequency at constant room temperature due to the material's polarization response characteristics. At lower frequencies, the dipoles within the material can reorient themselves in alignment with the changing electric field, which causes dielectric constant to increase. When frequency increases, the dipoles can't reorient quickly to keep up with the mi electric field. This lag in the dipole response reduces the material's overall polarization, leading to a decrease in the dielectric constant. This behaviour is related to the intrinsic relaxation times of their polarizable components. Figure 6(b). shows that at room temperature, the AC conductivity of g-C_3N_5 increases with an increase in frequency. This behaviour is explained by the polarization processes at work as well as the dielectric characteristics of the material. At lower frequencies, dipole polarization and other slow-moving charge carriers contribute less effectively to the overall conductivity. However, as the frequency rises, these dipoles and charge carriers are better able to align and respond to the alternating electric field, thus enhancing the material's ability to conduct AC electricity. Consequently, the material exhibits higher AC conductivity with increasing frequency due to the improved response of its charge carriers and polarization effects. The resulting Nyquist plot Figure 6(c) of g-C_3N_5 typically displays a semicircular curve. In this model, 'C', 'Q', and 'R' represent different components of the equivalent circuit: The letters "C", "Q" and "R" stand for bulk capacitance (C_b), constant phase element (CPE), and bulk resistance (R_b), respectively [42].

By fitting the experimental data to the (CQR) (CR) circuit, the values of C_b, Q, and R_b are determined, which describe the material's intrinsic electrical characteristics. The model allows for the extraction of grain-boundary properties, taking into account grain-boundary capacitance (C_{gb}) and resistance (R_{gb}). The semicircular nature of the Nyquist plot is indicative of the bulk material properties. The circuit parameter data for g-C_3N_5 at room temperature is shown in Table 1.

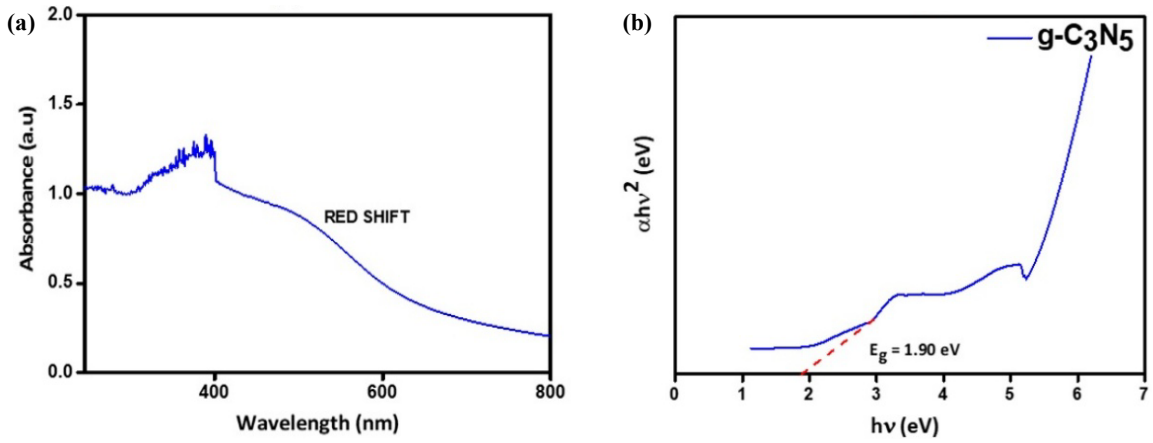

Figure 4. (a) UV-vis DRS spectra of g-C_3N_5, and (b) Band gap of g-C_3N_5.

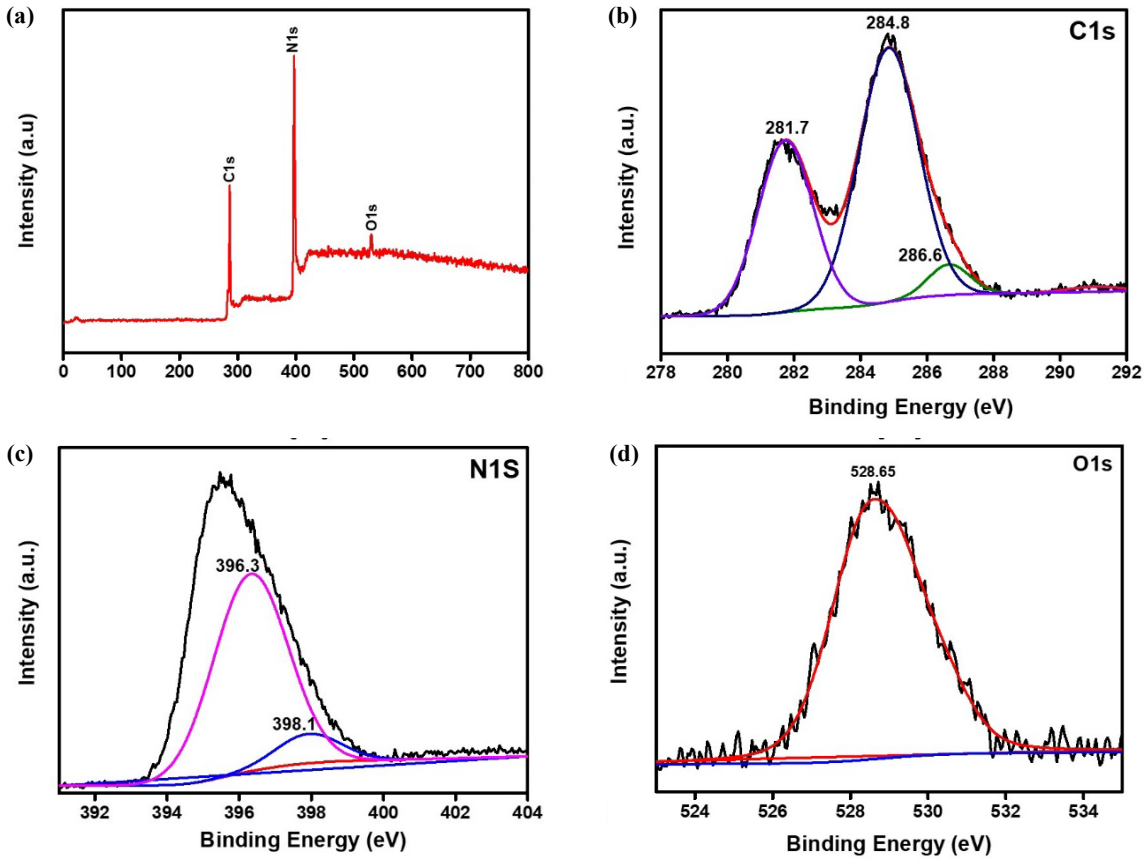

Figure 5. (a) XPS Survey curve of g-C_3N_5 and individual elemental spectrum of N1s, C1s, O1s, for g-C_3N_5 Nanosheet.

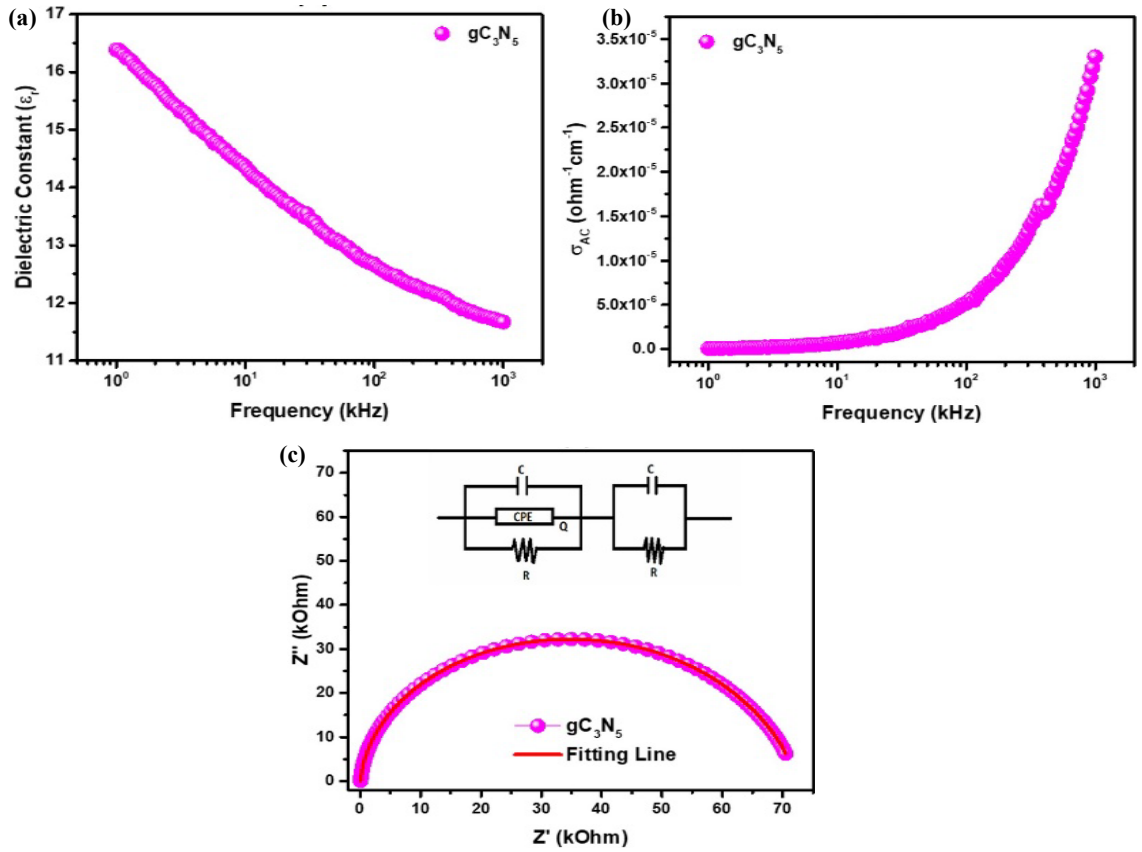

Figure 6. (a) Dielectric constant, (b) AC conductivity, and (c) Nyquist Plot for g-C_3N_5 nanosheet.

Table 1. Information on the circuit parameters of g-C_3N_5 at room temperature.

C_b [nF·cm^{-2}]	Q [S·sec^5·cm^{-2}]	n	R_b [ohm·cm^{-2}]	C_{gb} [F·cm^{-2}]	R_{gb} [ohm·cm^{-2}]
0.104	1.73×10^{-10}	0.92	6.79×10^{4}	1.73×10^{-8}	3.89×10^{3}

Table 2. Regression coefficient at different concentration of Malachite green.

Concentration [ppm]	Regression coefficient (R^2)	K_{app} [min^{-1}]
20	0.998	0.00876
40	0.990	0.00453
60	0.997	0.00223
80	0.997	0.00128

3.8 Degradation of Malachite Green (MG) using photocatalysis

g-C_3N_5 was used to photo catalytically decolourise Malachite green (MG) (Loba chemicals, 88% purity) in a solar light source. To set up a standard batch reaction, 0.02 g of catalyst was discharged in 20 mL of 20 ppm MG. To attain adsorption-desorption equilibrium, the dye solution was left in the dark before being exposed to sunlight [43]. After the reaction was first monitored in the dark for 30 min, the solution was let to stand in the sun for 90 min. g-C_3N_5 was used to observe the absorption spectrum within the 500 nm to 700 nm range at varying time intervals. At 614 nm, the significant MG absorption peak was detected and as the time got higher, it gradually declined. The lowest absorption peak was observed at 90 min as showed in Figure 7(a). The temporal evolution of dye concentration was shown using time-series monitoring. A notable decolourisation took place in less than 90 min, suggesting that most of the dye has been adsorbed onto the catalyst's surface. In the process of photocatalytic decolorization, pH is crucial. Figure 7(b) illustrates how the experiment was conducted at various pH intervals (2.5, 4.5, 6.5 and 8.5) to assess the impact of pH on the pace of the reaction. With a pH increase, the rate of photocatalytic decolorization gradually rises and then falls at higher pH values. The maximum photocatalytic decolorization of MG was seen at pH 6.5 as shown in Figure 7(c). It concludes that the degradation occurs in slightly basic range, which is due to influence of surface state of the catalyst and ionization state of the MG (Catanionic dye). This can be more defined as the adsorption of MG on surface of g-C_3N_5 depends on its surface charge. The g-C_3N_5 has high Pzc, when the pH < Pzc, g-C_3N_5 becomes positively charged in acidic medium, as a result of which there is decrease in less availability of active sites for adsorption of MG and at pH > Pzc the surface of g-C_3N_5 is negatively charged. So, in pH 6.5 causing the formation of hydroxyl group at g-C_3N_5 was increased. This ultimately facilitates the adsorption of MG on surface and causing degradation of MG [44]. To check the reaction kinetics, which was studied to confirm the above interpretation, was shown in Figure 7(d) by different concentration solutions (20, 40, 60, and 80 ppm) at various time intervals (15, 30, 45, 60, and 90 min). With a rate that is directly proportional to irradiation duration, the reaction exhibits Pseudo-first order kinetics.

$$\log\frac{Co}{C} = \frac{K_{app}}{2.303} \tag{5}$$

$$K_{app} = \log\frac{C_0}{C} \times 2.303 \times t \tag{6}$$

C_0 and C are the starting and ending concentrations of the MG solution, and K_{app} determines the pseudo first order reaction kinetics. Table 2 represents the apparent rate constant for MG and reveals that co- relation co-efficient (R_2) is almost equal to 1, indicating that the kinetic model is an appropriate fit for explaining the degradation of MG. Again, the photocatalytic decolorization procedure was carried out by adjusting the catalyst concentration from 0.02 g to 1 g in order to illustrate the ideal amount of catalyst dosage. The photocatalytic decolorization was found to increase gradually up to a concentration of 0.06 g, after which it remains constant Figure 7(e). This phenomenon is primarily driven by synergistic interaction between catalyst dosage and photoabsorbance. Since photoabsorbance rises with catalyst dose, more reactive molecules are available, which improves Malachite green (MG) photocatalytic decolourisation. As more catalyst is used, it has been seen that the percentage of photocatalytic decolorization stays constant. The reason behind this is that photocatalytic decolorization remains unaltered because there are no more molecules available to react and adsorb MG. The purpose of quenching study is to identify the active oxidative species responsible for the photocatalytic decolorization process. Various quenchers at 1 mM, such as parabenzoquinone, citric acid, DMSO, and isopropanol, were added in order to determine the potential reactive species, which include $O_2^{-\bullet}$, h^+, e^- and $OH^\bullet$, radicals. Based on the analysis, the highest reaction rate was achieved by the addition of parabenzoquinone and the highest rate of photocatalytic decolourisation was resulted in addition of iso-propanol. This experiment demonstrates that, out of all the oxidative radicals, $OH^\bullet$ radicals are the most likely reactive species for the decolorization process, in comparison to h^+, e^-, and $O_2^{-\bullet}$ as shown in Figure 7(f). To check the stability of g-C_3N_5 at pH 6.5 and in 20 ppm of MG reusability study was carried out. It was found that the catalyst was not been leached out even for five runs as shown in Figure 7(g).

3.8.1 Photocatalytic mechanistic pathway

To understand the possible mechanism behind photodegradation of malachite green (MG) by g-C_3N_5, the band levels of g-C_3N_5 were calculated using Equation (7-8).

$$E_{VB} = \chi - E_e + \left[\left(\frac{1}{2}\right) \times E_g\right] \tag{7}$$

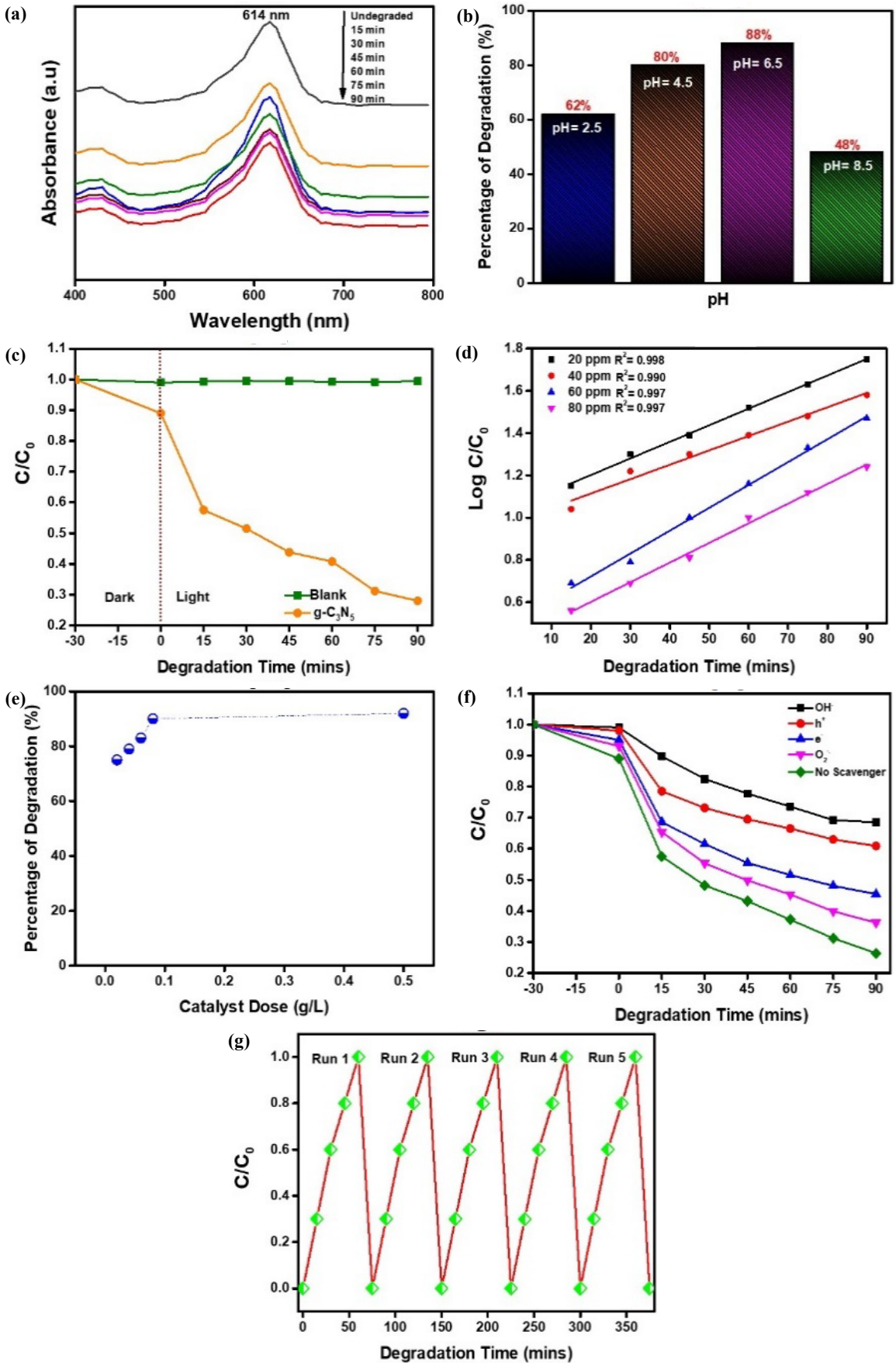

Figure 7. (a) Adsorption-desorption curve for MG over g-C_3N_5 nanosheet with respect to time, (b) Comparison of MG decolourisation rate at various pH values, (c) Degradation of MG by the g-C_3N_5 nanosheet, (d) Pseudo- 1st order MG decolourization kinetic figure at various concentrations, (e) Percentage of decolourisation of MG over catalyst dose, (f) Impact of active species on MG elimination, and (g) Reusability of g-C_3N_5 nanosheet for five cycles.

Table 3. Comparison table of g-C_3N_5 and based heterojunction for degradation of organic dyes.

Catalyst	Catalyst dosage	Dye	Initial dye concentration	Light source	Time [min]	Efficiency [%]	Ref.
g-C_3N_s/WO_3	0.16 g·L^{-1}	BG	15 ppm	Visible	60	99.4	[45]
g-C_3N_5	0.5 g·L^{-1}	MB	2.5 mg·L^{-1}	Visible	40	95	[28]
g-C_3N_5/g-C_3N_4	0.4 g·L^{-1}	RhB	10 mg·L^{-1}	Visible	30	98	[46]
g-C_3N_5/AgCl	1 g·L^{-1}	RhB	10 mg·L^{-1}	UV-Visible	30	96	[47]
g-C_3N_5/CeO_2	0.1 g·L^{-1}	RhB	10 mg·L^{-1}	Visible	30	71	[48]
g-C_3N_5	0.02 mg	MG	20 ppm	Visible	90	88	This work

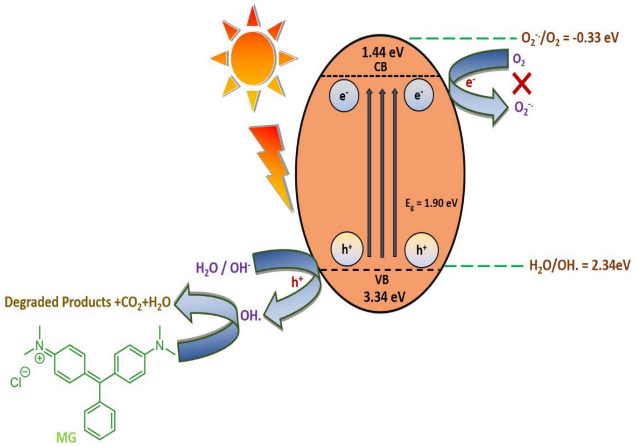

Figure 8. Photodegradation of malachite green (MG) by g-C_3N_5 Nanosheet.

$$E_{CB} = E_{VB} - E_g \quad (8)$$

Where E_g is the established band gap from the Tauc plot 1.90 eV for g-C_3N_5, E_e– Free electron energy measured using the hydrogen scale that is 4.5 eV, χ is the Mulliken electronegativity which is 6.89 for g-C_3N_5. These calculations revealed that the valence band potential E_{VB} was 3. 34 eV and the conduction band potential E_{CB} was 1.44 eV.

When g-C_3N_5 is exposed to light energy that exceeds its band gap energy, the photogenerated electrons jump from valence band (VB) to conduction band (CB) creating electron-hole (e^- - h^+) pairs. The holes formed in the VB will interact with surface water molecule or hydroxide ions to generate hydroxyl radicals OH• since the valence band potential is greater than the hydroxyl radicals' oxidation potential (OH•/H_2O –2.34 eV), the malachite green molecules are been transformed into CO_2 and H_2O through the of hydroxyl radicals. On the other hand, superoxide radicals ($O_2^{-\bullet}$) are not generated when photogenerated electrons react with atmospheric oxygen because the conduction band potential is lower than the reduction potential of ($O_2^{-\bullet}$/O_2). Therefore, the degradation of malachite green is attributed to photooxidation by hydroxyl radicals (OH•). The potential pathway for the photocatalytic decolorization process is shown in Figure 8 and described in Equation (9-11).

$$g\text{-}C_3N_5 + h\upsilon \rightarrow h^+(VB) + e^- (CB) \quad (9)$$

$$H_2O/OH^- + h^+ \rightarrow OH^\bullet \quad (10)$$

$$OH^\bullet + MG \rightarrow \text{Degraded Products} + CO_2 + H_2O \quad (11)$$

The mineralisation process through TOC showed the extend to degradation of malachite green by g-C_3N_5 was about 62% after 90 min of the reaction cycle, before it was of about 12% this confirms decolourization of the malachite green.

4. Conclusion

The thermally processed NH_4Cl and nitrogen rich precursor were combined to prepare g-C_3N_5 nanosheets which were subsequently protonated. The resulting g-C_3N_5 nanosheet exhibited outstanding photocatalytic performance, achieving 88% degradation of malachite green with rate constant of 0.00876 min^{-1} over 90 min. The augmented photoactivity was ascribed to the facial charge transfer dynamics, as corroborated by a suite of characterizations techniques. Trapping studies confirmed that the degradation of Malachite green was primarily induced by hydroxyl radical (OH•). Furthermore, the material demonstrated excellent stability, maintaining its performance over five consecutive runs, highlighting its potential as an efficient catalyst for the removal of the cationic dye Malachite green.

References

[1] R. Jasrotia, Suman, A. Verma, R. Verma, S. K. Godara, J. Ahmed, A. Mehtab, T. Ahmad, P. Puri, and S. Kalia, "Photocatalytic degradation of Malachite green pollutant using novel dysprosium modified Zn--Mg photocatalysts for wastewater remediation," *Ceramics International*, vol. 48, no. 19, pp. 29111-29120, 2022.

[2] L. Zeng, L. Xiao, Y. Long, and X. Shi, "Trichloroacetic acid-modulated synthesis of polyoxometalate@UiO-66 for selective adsorption of cationic dyes," *Journal of Colloid and Interface Science*, vol. 516, pp. 274-283, 2018.

[3] Y. Yang, G. Wang, B. Wang, L. Du, X. Jia, and Y. Zhao, "Decolorization of Malachite green by a newly isolated Penicillium sp. YW 01 and optimization of decolorization parameters," *Environmental Engineering Science,* vol. 28, no. 8, pp. 555-562, 2011.

[4] X. Yang, Y. Qin, L. Wei, and J. Yang, "Preparation of AgBr/g-C_3N_5 composite and its enhanced photodegradation for dyes," *Inorganic Chemistry Communications*, vol. 155, p. 110996, 2023.

[5] S. Liu, Y. Bu, S. Cheng, Y. Tao, and W. Hong, "Preparation of g-C_3N_5/g-C_3N_4 heterojunction for methyl orange photo-catalytic degradation: Mechanism analysis," *Journal of Water Process Engineering*, vol. 54, p. 104019, 2023.

[6] M. Tasbihi, A. Acharjya, A. Thomas, M. Reli, N. Ambrozova, K. Kocci, and R. Schomacker, "Photocatalytic CO_2 reduction by mesoporous polymeric carbon nitride photocatalysts," *Journal of Nanoscience and Nanotechnology*, vol. 18, no. 8, pp. 5636-5644, 2018.

[7] A. Subhadarshini, S. K. Samal, A. Pattnaik, and B. Nanda, "Facile fabrication of plasmonic Ag/ZIF-8: An efficient catalyst for investigation of antibacterial, haemolytic and photocatalytic degradation of antibiotics," *RSC Advances*, vol. 13, no. 45, pp. 31756-31771, 2023.

[8] A. Subhadarshini, E. Subudhi, P. G. R. Achary, S. A. Behera, N. Parwin, and B. Nanda, "ZIF-8 supported Ag_3PO_4/g-C_3N_4 a Double Z-scheme heterojunction: An efficient photocatalytic, antibacterial and hemolytic nanomaterial," *Journal of Water Process Engineering*, vol. 65, p. 105901, 2024.

[9] B. Nanda, S. A. Behera, A. Subhadarshini, P. M. Mishra, and P. G. R. Achary, "Sunlight assisted photocatalytic degradation of antibiotics by boron-doped lanthanum ferrite," *Journal of Molecular Structure*, vol. 1306, p. 137921, 2024.

[10] S. Li, C. You, F. Yang, G. Liang, C. Zhuang, and X. Li, "Interfacial Mo–S bond modulated S-scheme $Mn_{0.5}Cd_{0.5}S$/Bi_2MoO_6 hetero-junction for boosted photocatalytic removal of emerging organic contaminants," *Chinese Journal of Catalysis*, vol. 68, pp. 259-271, 2025.

[11] S. Li, K. Rong, X. Wang, C. Shen, F. Yang, and Q. Zhang, "Design of carbon quantum dots/CdS/Ta_3N_5 S-scheme heterojunction nanofibers for efficient photocatalytic antibiotic removal," *Acta Physico-Chimica Sinica,* vol. 40, no. 12, p. 2403005, 2024.

[12] C. Shen, X. Li, B. Xue, D. Feng, Y. Liu, F. Yang, M. Zhang, and S. Li, "Surface plasmon effect combined with S-scheme charge migration in flower-like Ag/$Ag_6Si_2O_7$/$Bi_{12}O_{17}Cl_2$ enables efficient photocatalytic antibiotic degradation," *Applied Surface Science*, vol. 679, p. 161303, 2025.

[13] S. Li, R. Yan, M. Cai, W. Jiang, M. Zhang, and X. Li, "Enhanced antibiotic degradation performance of $Cd_{0.5}Zn_{0.5}S$/Bi_2MoO_6 S-scheme photocatalyst by carbon dot modification," *Journal of Materials Science & Technology*, vol. 164, pp. 59-67, 2023.

[14] C. Wang, K. Rong, Y. Liu, F. Yang, and S. Li, "Carbon quantum dots-modified tetra (4-carboxyphenyl) porphyrin/ BiOBr S-scheme heterojunction for efficient photocatalytic antibiotic degradation," *Science China Materials*, vol. 67, no. 2, pp. 562-572, 2024.

[15] M. Soto-Hernandez, M. Palma-Tenango, and M. del Rosario Garcia-Mateos, "Phenolic compounds: Natural sources, importance and applications." *IntechOpen*, 2017.

[16] P. Ju, Y. He, M. Wang, X. Han, F. Jiang, C. Sun, and C. Wu, "Enhanced peroxidase-like activity of MoS_2 quantum dots functionalized g-C_3N_4 nanosheets towards colorimetric detection of H2O2," *Nanomaterials*, vol. 8, no. 12, p. 976, 2018.

[17] A. Thomas, A. Fischer, F. Goettmann, M. Antonietti, J-O. Müller, R. Schlögl, and J. M. Carlsson, "Graphitic carbon nitride materials: Variation of structure and morphology and their use as metal-free catalysts," *Journal of Materials Chemistry*, vol. 18, no. 41, pp. 4893-4908, 2008.

[18] X. Yang, Y. Ye, J. Sun, Z. Li, J. Ping, and X. Sun, "Recent advances in g-C_3N_4-based photocatalysts for pollutant degradation and bacterial disinfection: design strategies, mechanisms, and applications," *Small*, vol. 18, no. 9, p. 2105089, 2022.

[19] L. Huang, Z. Liu, W. Chen, D. Cao, and A. Zheng, "Two-dimensional graphitic C_3N_5 materials: Promising metal-free catalysts and CO_2 adsorbents," *Journal of Materials Chemistry A*, vol. 6, no. 16, pp. 7168-7174, 2018.

[20] Y. Cui, G. Zhang, Z. Lin, and X. Wang, "Condensed and low-defected graphitic carbon nitride with enhanced photocatalytic hydrogen evolution under visible light irradiation," *Applied Catalysis B: Environment and Energy*, vol. 181, pp. 413-419, 2016.

[21] P. Kumar, E. Vahidzadeh, U. K. Tahku, P. Kar, K. M. Alam, A. Goswami, N. Mahdi, K. Cui, G. M. Bernard, V. K. Michaelis, and K. Shankar, "C_3N_5: A low bandgap semiconductor containing an azo-linked carbon nitride framework for photocatalytic, photovoltaic and adsorbent applications," *Journal of the American Chemical Society*, vol. 141, no. 13, pp. 5415-5436, 2019.

[22] J. Zhang, G. Yu, C. Yang, and S. Li, "Recent progress on S-scheme heterojunction strategy enabling polymer carbon nitrides C_3N_4 and C_3N_5 enhanced photocatalysis in energy conversion and environmental remediation," *Current Opinion in Chemical Engineering*, vol. 45, p. 101040, 2024.

[23] J. Zhang, C. Yang, H. Liu, G. Yu, Z. Duan, and S. Li, "Insights into interfacial S-scheme/bulk type II dual charge transfer mechanism enabling silver oxide/N-rich carbon nitride anti-photocorrosion and enhanced photoactivity," *Applied Catalysis B: Environment and Energy*, vol. 349, p. 123883, 2024.

[24] J. Zhang, W. Liu, B. Liu, X. Duan, Z. Ao, and M. Zhu, "Is single-atom catalyzed peroxymonosulfate activation better? Coupling with metal oxide may be better," *Chinese Journal of Catalysis*, vol. 59, pp. 137-148, 2024.

[25] I. Y. Kim, S. Kim, X. Jin, S. Pramkumar, G. Chandra, N-S. Lee, G. P. Mane, S-J. Hwang, S. Umapathy, and A. Vinu, "Ordered mesoporous C_3N_5 with a combined triazole and triazine framework and its graphene hybrids for the oxygen reduction reaction (ORR)," *Angewandte Chemie*, vol. 130, no. 52, pp. 17381-17386, 2018.

[26] C. Tian, S. Liu, M. Shao, and Y. Bu, "Preparation of g-C_3N_5 composites for butyl xanthate photocatalytic degradation," *Inorganic Chemistry Communications*, vol. 159, p. 111726, 2024.

[27] Q. Li, S. Song, Z. Mo, L. Zhang, Y. Qian, and C. Ge, "Hollow carbon nanospheres@graphitic C_3N_5 heterostructures for enhanced oxygen electroreduction," *Applied Surface Science*, vol. 579, no. 44, p. 152006, 2022.

[28] T. Liu, G. Yang, W. Wang, C. Wang, M. Wang, X. Sun, P. Xu, and J. Zhang, "Preparation of C_3N_5 nanosheets with enhanced performance in photocatalytic methylene blue (MB) degradation and H_2-evolution from water splitting," *Environmental Research*, vol. 188, p. 109741, 2020.

[29] H. Wang, M. Li, Q. Lu, Y. Cen, Y. Zhang, and S. Yao, "A mesoporous rod-like g-C_3N_5 synthesized by salt-guided strategy:

As a superior photocatalyst for degradation of organic pollutant," *ACS Sustainable Chemistry & Engineering*, vol. 7, no. 1, pp. 625-631, 2018.

[30] L. T. Tai, D. N. Minh, N. Nguyen, A. Hoang, L. M. Huong, C. Q. Cong, N. D. Hai, P. T. Mai. and H. H. Nguyen, "Green synthesis of copper oxide nanoparticles for photodegradation of malachite green and antibacterial properties under visible light," *Optical Materials*, vol. 136, p. 113489, 2023.

[31] Q. Meng X. Yang, L. Wu, T. Chen, Y. Li, R. He, W. Zhu, L. Zhu, and T. Duan, "Metal-free 2D/2D C_3N_5/GO nanosheets with customized energy-level structure for radioactive nuclear wastewater treatment," *Journal of Hazardous Materials*, vol. 422, p. 126912, 2022.

[32] A. Subhadarshini, S. K. Samal, and B. Nanda, "Z-Scheme heterojunction-based rod-shaped g-C_3N_5/ZIF-8: Enhancing photocatalytic, antibacterial and hemolytic activity," *Journal of Inorganic and Organometallic Polymers and Materials,* pp. 1-15, 2024.

[33] D.-H. Park, K. S. Lakhi, K. Ramadass, M-K. Kim, S. N. Talapaneni, S. Joseph, U. Ravon, K. Bahily-Al, and A. Vinu, "Energy efficient synthesis of ordered mesoporous carbon nitrides with a high nitrogen content and enhanced CO_2 capture capacity," *Chemistry – A European Journal*, vol. 23, no. 45, pp. 10753-10757, 2017.

[34] S. Cai, X. Zuo, H. Zhao, S. Yang, R. Chen, L. Chen, R. Zhang, D. Ding, and T. Cai, "Evaluation of N-doped carbon for the peroxymonosulfate activation and removal of organic contaminants from livestock wastewater and groundwater," *Journal of Materials Chemistry A*, vol. 10, no. 16, pp. 9171-9183, 2022.

[35] X. Liu, S. Xing, Y. Xu, R. Chen, C. Lin, and L. Guo, "3-amino-1,2,4-triazole-derived graphitic carbon nitride for photodynamic therapy," *Spectrochimica Acta, Part A: Molecular and Biomolecular Spectroscopy*, vol. 250, p. 119363, 2021.

[36] W. Liao, Z. Yang, Y. Wang, S. Li, C. Wang, and Z. Zhou, "Novel Z-scheme Nb_2O_5/C_3N_5 photocatalyst for boosted degradation of tetracycline antibiotics by visible light-assisted activation of persulfate system," *Chemical Engineering Journal*, vol. 478, p. 147346, 2023.

[37] S. A. Behera, A. Amanat, and P. G. R. Achary, "Photocatalytic degradation of ciprofloxacin drug utilizing novel PVDF/polyaniline/lanthanum strontium manganate@ Ag composites," *Journal of Metals, Materials and Minerals*, vol. 34, no. 1, p. 1896, 2024.

[38] S. A. Behera, A. Subhadarshini, S. S. Bhuyan, B. Nanda, and P. G. R. Achary, "PVDF/rGO/CuO nanocomposites: A robust platform for solar-driven tetracycline photodegradation," *Inorganic Chemistry Communications*, vol. 160, p. 111995, 2024.

[39] S. A. Behera, D. Khatua, R. K. Singh, R. N. P. Choudhary, and P. G. R. Achary, "Temperature-dependent electrical and dielectric characteristics of lead germanate $Pb_5Ge_{1.5}Sn_{1.5}O_{11}$," *Inorganic Chemistry Communications*, vol. 163, p. 112370, 2024.

[40] Z. Cai, Y. Huang, H. Ji, W. Liu, J. Fu, and X. Sun, "Type-II surface heterojunction of bismuth-rich $Bi_4O_5Br_2$ on nitrogen-rich g-C_3N_5 nanosheets for efficient photocatalytic degradation of antibiotics," *Separation and Purification Technology*, vol. 280, p. 119772, 2022.

[41] C. You, C. Wang, M. Cai, Y. Liu, B. Zhu, and S. Li, "Improved photo-carrier transfer by an internal electric field in BiOBr/ Nrich C_3N_5 3D/2D S-scheme heterojunction for efficiently photocatalytic micropollutant removal," *Acta Physico-Chimica Sinica*, vol. 40, no. 11, p. 2407014, 2024.

[42] R. Shyam, A. Kumar, S. Pal, and R. Prakash, "Investigation of palladium-doped 2D g-C_3N_5 materials for enhanced electrocatalytic activity towards hydrogen evolution reaction," *Electrochimica Acta*, vol. 496, p. 144485, 2024.

[43] Y. Li, X. Wang, X. Wang, Y. Xia, A. Zhang, J. Shi, L. Gao, H. Wei, and W. Chen, "Z-scheme $BiVO_4$/g-C_3N_4 heterojunction: An efficient, stable and heterogeneous catalyst with highly enhanced photocatalytic activity towards Malachite Green assisted by H_2O_2 under visible light," *Colloids and Surfaces A Physicochemical and Engineering Aspects*, vol. 618, p. 126445, 2021.

[44] L. Saikia, D. Bhuyan, M. Saikia, B. Malakar, D. K. Dutta, and P. Sengupta, "Photocatalytic performance of ZnO nanomaterials for self sensitized degradation of malachite green dye under solar light," *Applied Catalysis A: General*, vol. 490, pp. 42-49, 2015.

[45] B. Hazarika, B. Bhattacharjee, and M. Ahmaruzzaman, "Enhanced photocatalytic degradation of brilliant green using g-C_3N_5/WO_3 nanocomposite: A Z-scheme charge transfer approach under visible light irradiation," *Inorganic Chemistry Communications*, vol. 168, p. 112960, 2024.

[46] F. Yi, J. Liu, G. Liang, X. Xiao, and H. Wang, "Insight into the enhanced degradation mechanism of g-C_3N_4/g-C_3N_5 heterostructures through photocatalytic molecular oxygen activation in Van der Waals junction and excitation," *Journal of Alloys and Compounds*, vol. 905, p. 164064, 2022.

[47] S. Vadivel, H. Ganesh, B. Paul, S. Rajendran, A. Habibi-Yangjeh, M. Duraisamy, and M. Kumaravel, "Synthesis of novel AgCl loaded g-C_3N_5 with ultrahigh activity as visible light photocatalyst for pollutants degradation," *Chemical Physics Letters*, vol. 738, p. 136862, 2019.

[48] J. Yang, J. Long, J. Wang, H. Zhang, X. Yang, and L. Wei, "Synthesis of visible-light driven CeO_2/g-C_3N_5 heterojunction with enhanced photocatalytic performance for organic dyes," *Journal of Physics and Chemistry of Solids*, vol. 187, no. 1, p. 111867, 2024.